

Article

SnS₂ Nanosheets as a Template for 2D SnO₂ Sensitive Material: Nanostructure and Surface Composition Effects

Roman Vasiliev^{1,2}, Darya Kurtina¹, Nataliya Udalova², Vadim Platonov¹, Abulkosim Nasriddinov^{1,2} , Tatyana Shatalova¹, Roman Novotortsev¹, Xiaogan Li³ and Marina Rumyantseva^{1,*} 

¹ Chemistry Department, Moscow State University, 119991 Moscow, Russia

² Faculty of Materials Science, Moscow State University, 119991 Moscow, Russia

³ School of Microelectronics, Key Lab of Liaoning for Integrated Circuits Technology, Dalian University of Technology, Dalian 116024, China

* Correspondence: room@inorg.chem.msu.ru

Abstract: Two-dimensional nanosheets of semiconductor metal oxides are considered as promising for use in gas sensors, because of the combination of a large surface-area, high thermal stability and high sensitivity, due to the chemisorption mechanism of gas detection. In this work, 2D SnO₂ nanosheets were synthesized via the oxidation of template SnS₂ nanosheets obtained by surfactant-assisted one-pot solution synthesis. The 2D SnO₂ was characterized using transmission and scanning electron microscopy (TEM, SEM), X-ray diffraction (XRD), low-temperature nitrogen adsorption, X-ray photoelectron spectroscopy (XPS) and IR spectroscopy. The sensor characteristics were studied when detecting model gases CO and NH₃ in dry (RH₂₅ = 0%) and humid (RH₂₅ = 30%) air. The combination of high specific-surface-area and increased surface acidity caused by the presence of residual sulfate anions provides a high 2D SnO₂ sensor's signal towards NH₃ at a low temperature of 200 °C in dry air, but at the same time causes an inversion of the sensor response when detecting NH₃ in a humid atmosphere. To reveal the processes responsible for sensor-response inversion, the interaction of 2D SnO₂ with ammonia was investigated using diffuse reflectance infrared Fourier transform spectroscopy (DRIFTS) in dry and humid air at temperatures corresponding to the maximum “positive” and maximum “negative” sensor response.

Keywords: 2D nanomaterials; template synthesis; SnS₂ nanosheets; SnO₂ nanosheets; gas sensor; carbon monoxide; ammonia



Citation: Vasiliev, R.; Kurtina, D.; Udalova, N.; Platonov, V.; Nasriddinov, A.; Shatalova, T.; Novotortsev, R.; Li, X.; Rumyantseva, M. SnS₂ Nanosheets as a Template for 2D SnO₂ Sensitive Material: Nanostructure and Surface Composition Effects. *Materials* **2022**, *15*, 8213. <https://doi.org/10.3390/ma15228213>

Academic Editors: Lin Qiu, Jie Lin, Changyong Gao and Xiaotian Wang

Received: 7 November 2022

Accepted: 17 November 2022

Published: 18 November 2022

Publisher's Note: MDPI stays neutral with regard to jurisdictional claims in published maps and institutional affiliations.



Copyright: © 2022 by the authors. Licensee MDPI, Basel, Switzerland. This article is an open access article distributed under the terms and conditions of the Creative Commons Attribution (CC BY) license (<https://creativecommons.org/licenses/by/4.0/>).

1. Introduction

Two-dimensional (2D) semiconductor nanomaterials have attracted a great deal of research interest due to their unique dimension-dependent electronic properties. Two-dimensional semiconductors may find a variety of applications, such as high-mobility transistors [1] and sensitive photodetectors [2], as well as gas sensors [3,4]. The family of 2D materials significantly increased in 2010–2020, and now includes materials that are diverse in nature: phosphorene, an analog of graphene consisting of atomically thin layers of phosphorus [5,6]; a group of materials with the common name MXenes, including 2D carbides, nitrides and carbonitrides [7,8]; boron nitride [9]; molybdenum, tungsten and rhenium dichalcogenides [10,11]; layered semiconductor chalcogenides GaS, GaSe, SnS₂ [12–14] and layered oxides (MoO₃) [15]. It should be noted that for practical application in the field of gas sensors, 2D materials such as graphene and its derivatives or MoS₂, MoSe₂, WS₂, WSe₂ have a number of significant limitations [16–18]. The main disadvantage of 2D materials is their low stability and fully saturated surface. Temperature rise and thermal cycling in air, to clean the surface of layered chalcogenides, phosphorene, and carbides (MXenes) leads to surface oxidation, degradation of adsorption properties and increased resistance. A common disadvantage of 2D materials is their reasonably low

sensitivity due to the primary contribution of physical adsorption instead of chemisorption into the sensor signal.

The 2D nanosheets of semiconductor metal oxides may be considered as promising for use in gas sensors, since the combination of a large surface-area, high thermal stability and high sensitivity, due to the chemisorption mechanism of gas detection, is expected. However, the semiconductor oxides ZnO, SnO₂, In₂O₃, WO₃, most commonly used as gas-sensitive materials, do not have a layered structure, which makes it difficult to synthesize them in the form of 2D nanosheets by traditional methods such as the exfoliation route. For example, various methods of hydrothermal synthesis have been proposed to obtain SnO₂ [19–26], but they allow the acquirement only of hierarchical 3D structures (of the nanoflowers type) formed by 2D nanosheets. An interesting example is the synthesis of 2D indium oxide, InO, in the spatial confinement between SiC and graphene using the MOCVD method [27]. It was found that the predicted atomic arrangement of intercalated In atoms is consistent with the In–In distances predicted for the stable 2D InO structure [28]. The authors of [28] also reported on the structural and electronic properties of In₂O₃ 2D structures with planar hexagonal geometry.

An alternative approach may be template synthesis, in which 2D nanosheets of layered sulfide are oxidized to form an oxide while preserving the morphology of the particles. The recent works in this direction are the articles by V. Paolucci et al. [29,30], presenting SnSe₂ 2D nanosheets as a template for obtaining amorphous SnO₂ layers.

Tin disulfide SnS₂, a widely known layered material, is an indirect semiconductor with an energy gap of approximately 2.07 eV [31]. It has attracted interest in photovoltaic [32], photocatalytic [33,34] and sensor [35] applications and also as a material for Li-ion batteries [36,37]. Recently, SnS₂ nanoparticles with a morphology of nanoflowers [33,34] or nanosheets [36,37] were synthesized using surfactant-assisted hydrothermal routes. Growth of SnS₂ nanoplatelets in nonpolar solutions using the solvothermal method starting from SnCl₄·5H₂O [32] or by the thermal decomposition of Sn(S₂CNEt₂)₄ single-molecular precursor [38] with the use of oleylamine as the surfactant, was reported.

Here, we report a simple method of producing 2D SnO₂ nanosheets via the oxidation of template SnS₂ nanosheets obtained by surfactant-assisted one-pot solution synthesis. The 2D SnO₂ was characterized in detail, in terms of microstructure parameters and surface composition, and also tested as a gas-sensitive material when detecting CO and NH₃.

2. Materials and Methods

All chemicals were purchased from Sigma Aldrich in the purest form available and used for the syntheses without further purification.

Colloidal SnS₂ nanosheets were synthesized under argon atmosphere, following the protocol outlined here. Tin (IV) acetate Sn(CH₃COO)₄ (0.023 mmol) and oleic acid (0.09 mmol) were added to 1-octadecene (2 mL) followed by heating at 200 °C for approximately 1 h under argon flow to remove the acetic acid and form the tin oleate complex. The solution was then cooled to room temperature, and dodecylamine (0.09 mmol) and elemental sulfur (0.045 mmol) were added. The mixture was heated again to 220 °C under vigorous stirring and held at this temperature for approximately 5 min. As the desired temperature was reached, the initial colorless solution changed to yellow and then to turbid orange. The resultant solution was cooled, mixed with an equal volume of acetone, and centrifuged at 6000 rpm for 10 min. The supernatant was discarded, and the sediment nanosheets were redispersed in toluene. The SnS₂ nanosheets were additionally precipitated using an equal volume of acetone, separated by centrifugation, and redispersed in the toluene. The resultant orange dispersion was slightly turbid and was stable to aggregation for several days.

The conditions of complete SnS₂ to SnO₂ oxidative transformation were determined by thermogravimetric analysis with mass spectral analysis of gaseous products (TG-MS), using a NETZSCH STA 409 PC/PG instrument (heating in air, 5K/min) (Figure 1). The oxidation of organic stabilizers (oleic acid and dodecylamine) occurs in the temperature

range of 250–600 °C, as evidenced by a symbiotic increase in ionic currents, corresponding to the mass numbers $m/z = 18$ (H_2O), 44 (CO_2) and 30 (NO). The oxidation of sulfide anions, which is accompanied by the release of SO_2 ($m/z = 64$) occurs in a narrower temperature range of 250–550 °C. To obtain 2D SnO_2 , the SnS_2 sol was dried in air at room temperature until the solvent was removed. The SnS_2 powder was annealed at 500 °C for 6 h. The annealing temperature of 500 °C was chosen to obtain 2D SnO_2 with high specific-surface-area.

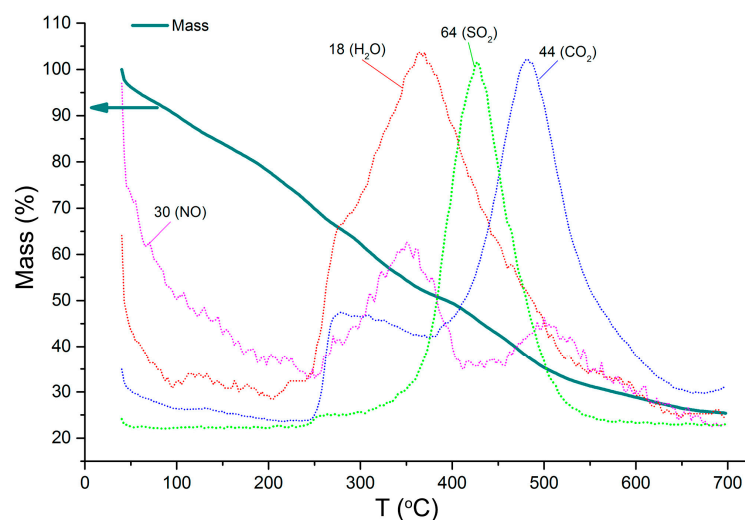


Figure 1. TG curve and temperature dependencies of ionic current for $m/z = 18$ (H_2O), 30 (NO), 44 (CO_2), 64 (SO_2) for SnS_2 oxidation in air.

The size and morphology of the SnS_2 nanoparticles were determined by transmission electron microscopy (TEM), with the LEO19 AB OMEGA microscope operated at 100 kV and the JEOL JEM2100 microscope operated at 200 kV. The morphology of the SnS_2 and 2D SnO_2 powders was studied with scanning electron microscopy (SEM), using a Carl Zeiss SUPRA 40 FE-SEM instrument with Inlens SE detector (accelerating voltage 5 kV, aperture 30 μm). The specific surface area of 2D SnO_2 was measured by the low-temperature nitrogen adsorption, using a Chemisorb 2750 instrument (Micromeritics).

The phase composition was analyzed using X-ray diffraction (XRD) and Raman spectroscopy. A Panalytical Aeris Research diffractometer ($\text{CuK}\alpha$ radiation, Bragg–Brentano geometry, PiXcel detector, with a total angular range of 3.000–60.000° 2θ , a step size of ca. 0.005° and variable exposure time) was used for X-ray-powder-diffraction measurements. For this investigation, concentrated solutions of the purified nanocrystals were spread on top of a silicon wafer. The SnO_2 crystallite size was estimated using the Scherrer formula. Raman spectra of SnS_2 were acquired on a Renishaw InVia Raman microscope equipped with a 514 nm argon laser. Raman spectra of 2D SnO_2 were collected on the i-Raman Plus spectrometer (BW Tek) equipped with a BAC 151C microscope and a 532 nm laser.

The surface composition was analyzed using X-ray photoelectron spectroscopy (XPS) and Fourier transform infrared (FTIR) spectroscopy. XP spectra were obtained on Omicron ESCA+ (monochromatic $\text{AlK}\alpha$ anode, $E = 1486.6$ eV) using a neutralizer (scanning step 0.1 eV/s, transmission energy 20 eV). The spectra were processed using the UNIFIT software. The peaks were approximated by convolution of the Gauss and Lorentz functions, with the simultaneous optimization of the background parameters. The FTIR spectra were registered in transmission mode using a Frontier (Perkin Elmer) spectrometer in the 4000–400 cm^{-1} region, with a step of 1 cm^{-1} . For these experiments, 0.3–0.5 mg of the powder was ground with 40 mg KBr (FT-IR grade, Sigma-Aldrich, St. Louis, MO, USA) and pressed into tablets (~0.5 mm thick, 12 mm in diameter). The baseline was preliminarily taken from pure KBr.

Diffuse reflectance infrared fourier-transformed (DRIFT) spectra were recorded on a Frontier (Perkin Elmer) spectrometer using a DiffusIR annex and heated-flow chamber HC900 (Pike Technologies, Fitchburg, WI, USA) sealed by a ZnSe window. DRIFT spectra were registered in the $4000\text{--}1000\text{ cm}^{-1}$ region with resolution 4 cm^{-1} and with accumulation of 30 scans with automatic $\text{H}_2\text{O}/\text{CO}_2$ compensation. The 2D SnO_2 powder (30 mg) was placed in alumina crucibles (5 mm diameter). The measurements were performed under $100\text{ mL}/\text{min}$ flow of dry (relative humidity at $25\text{ }^\circ\text{C}$ $\text{RH}_{25} = 0\%$) or humid ($\text{RH}_{25} = 30\%$) air, containing 100 ppm NH_3 at $200\text{ }^\circ\text{C}$ and at $350\text{ }^\circ\text{C}$.

To manufacture the 2D SnO_2 sensors, concentrated SnS_2 sol in toluene was deposited dropwise on the alumina substrates with Pt contacts and Pt heaters (Figure 2). To form a sensitive film, the deposition of SnS_2 was repeated three times. After each deposition, the layer was dried in air at room temperature until the solvent evaporated, and then slowly heated to $500\text{ }^\circ\text{C}$, using a substrate heater. To oxidize SnS_2 into 2D SnO_2 , the formed films were additionally annealed in air at $500\text{ }^\circ\text{C}$ for 6 h. The selected annealing temperature of $500\text{ }^\circ\text{C}$ allows for complete oxidation of the SnS_2 , and provides the necessary thermal stability of 2D SnO_2 during sensor measurements in the temperature range of $50\text{--}500\text{ }^\circ\text{C}$. Certified gas mixtures containing 2530 ppm CO in N_2 and 240 ppm NH_3 in N_2 were used as gas sources. The concentration of the target gas in the air was set and controlled using EL-FLOW mass-flow controllers (Bronkhorst). The flow rate through the measuring cell in all measurements was constant $100 \pm 0.5\text{ mL}/\text{min}$. The humidity of the gas mixture (relative humidity at $25\text{ }^\circ\text{C}$ $\text{RH}_{25} = 0\%$ for dry conditions and $\text{RH}_{25} = 30\%$ for humid conditions) was set and controlled by a P-2 Humidifier (Cellkraft). The sensor resistance was measured at 1.3 V DC -voltage at a temperature fixed in the range of $50\text{--}500\text{ }^\circ\text{C}$, with the step of $50\text{ }^\circ\text{C}$. For each temperature, three cycles of measurements (15 min in pure air, 15 min in the presence of air containing the target gas), were performed. The sensor response was calculated as $S = (G_{\text{gas}} - G_{\text{air}})/G_{\text{air}}$, where G_{air} is the sensor conductance in air, and G_{gas} is the sensor conductance in the CO - or NH_3 -containing gas mixture.

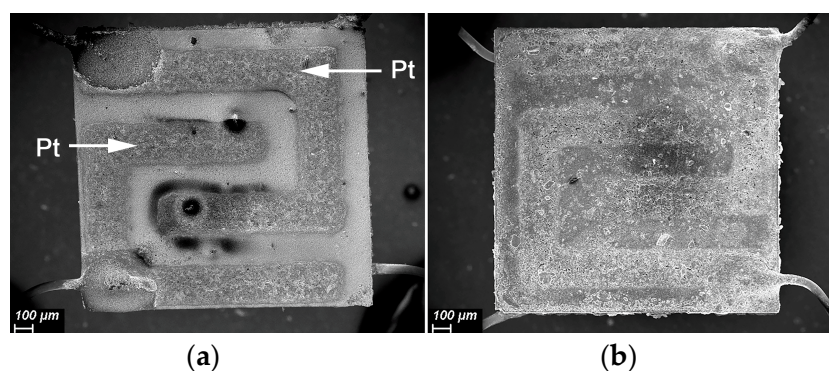


Figure 2. SEM image of alumina substrate with Pt contacts: (a) bare substrate, (b) covered with 2D SnO_2 .

3. Results

3.1. Microstructure, Phase Composition and Surface Composition

The nanosheet morphology was studied using the transmission and scanning electron microscopy (TEM and SEM) methods. Figure 3 shows a series of representative TEM images of the SnS_2 sample. The SnS_2 nanosheets have 2D morphology. The sample is formed by $\sim 5\text{ nm}$ thick nanosheets packed in agglomerates of 4–5 pieces (Figure 3b). The electron-diffraction pattern (inset in Figure 3a) taken from an ensemble of nanosheets shows that particles have the crystal structure of SnS_2 (berndtite). When oxidized at $500\text{ }^\circ\text{C}$, the structure of the 2D nanosheets is mostly preserved. (Figure 3c,d). SEM images (Figure 4) reveal the formation of nanosheets with lateral lengths $> 500\text{ nm}$.

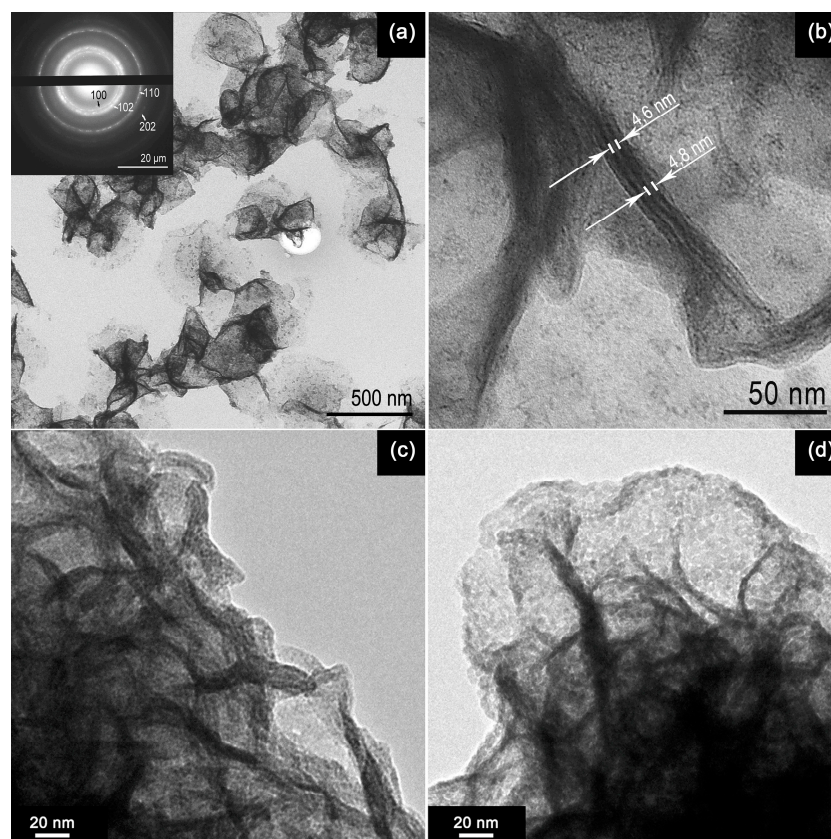


Figure 3. TEM images of SnS₂ nanosheets before (a–c) and after (d) oxidation at 500 °C. Inset shows the electron-diffraction pattern.

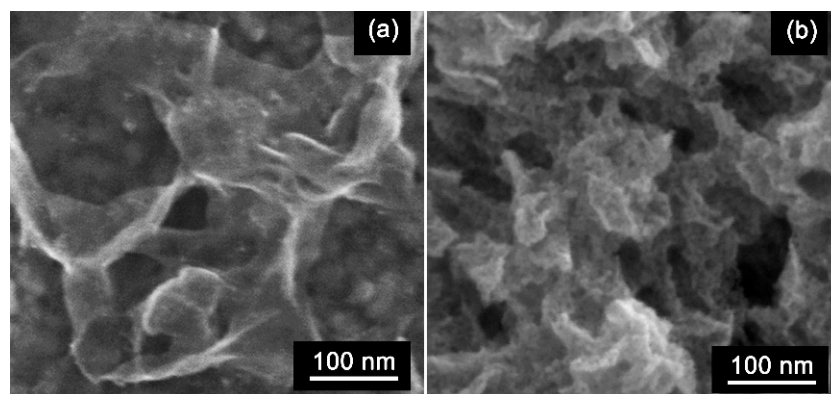


Figure 4. SEM images of SnS₂ nanosheets before (a) and after (b) oxidation at 500 °C.

The X-ray diffraction pattern of the SnS₂ nanosheets (Figure 5) is close to the diffractogram of the SnS₂ Berndtite-2T standard (ICDD No. 23-677). The diffraction pattern contains broadened reflections (100) and (110), which refer to the directions lying in the plane of the sheet. At the same time, the reflection (001) corresponding to the normal to the plane of the sheet does not appear. This may be due to the extremely small thickness of the sheet that indicates the implementation of a 2D structure. The oxidation of the SnS₂ nanosheets leads to the formation of SnO₂ with a cassiterite structure (ICDD No. 41-1445). The diffraction maxima of 2D SnO₂ are greatly broadened, which indicates the small size of the crystal grains. The crystallite size of the 2D SnO₂ calculated using Sherrer's formula with (110) and (101) reflections is 4.0 ± 0.5 nm, which correlates with the high specific area of 44 ± 2 m²/g.

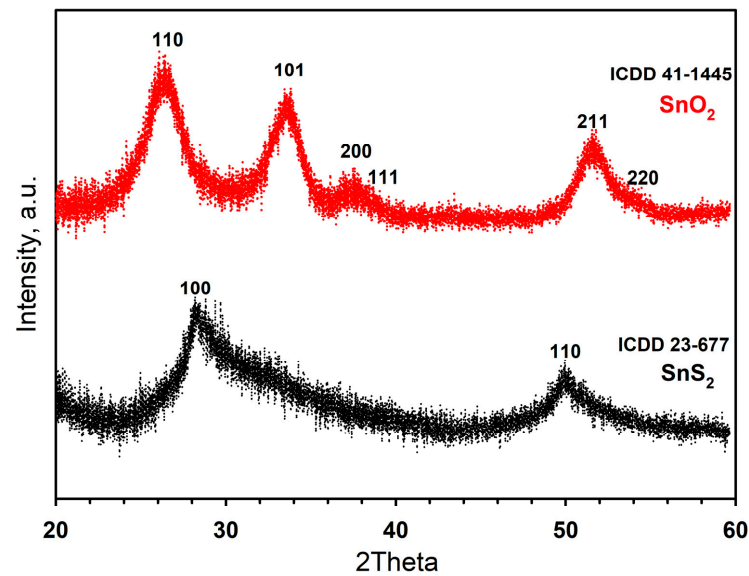


Figure 5. X-ray diffraction patterns of SnS₂ nanosheets and 2D SnO₂ powder.

Figure 6 compares the Raman spectra of the SnS₂ and 2D SnO₂ nanosheets. Assignments of Raman vibrational modes are presented in Table 1. Two peaks with maxima at 230 cm⁻¹ and 317 cm⁻¹ are observed in the Raman spectrum of the SnS₂ nanosheets (Figure 6a). The latter corresponds to the A_{1g} mode of SnS₂ [39]. The line at 230 cm⁻¹ is shifted towards large wavenumbers compared with E_g SnS₂ (205–210° cm⁻¹ for a single crystal [39,40]) and is very intense, compared with A_{1g}. Such modification of the spectrum may be due to the dimensional effect and the formation of a 2D structure [41]. In the Raman spectrum of the 2D SnO₂ sample (Figure 6b), there are A_{1g}, E_g, B_{2g}, B_{1g} tin dioxide modes as well as a wide band in the range of 400–700 cm⁻¹, corresponding to the superposition of surface modes [42]. The assignment of Raman bands corresponding to volume modes is made on the basis of the literature data [43]. The appearance of surface modes is associated with the small size of the SnO₂ particles, and may be due to the manifestation of symmetry-forbidden oscillations, due to a disturbance of the long-range order in systems of reduced dimension [42]. An alternative explanation is the formation of a highly defective near-surface layer, the contribution of which is maximal for materials with the smallest particle size [44]. In the range of 900–2000 cm⁻¹ in the spectrum of 2D SnO₂, there are lines corresponding to the residues of the oleic acid stabilizer used in the synthesis of the SnS₂ nanosheets (Table 1).

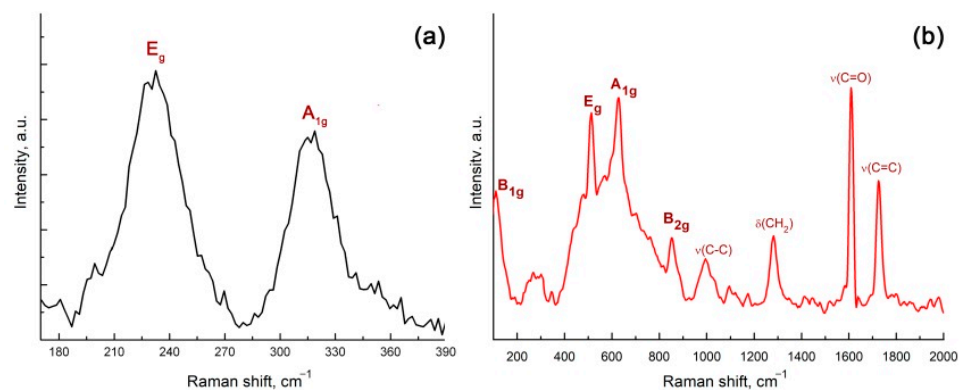
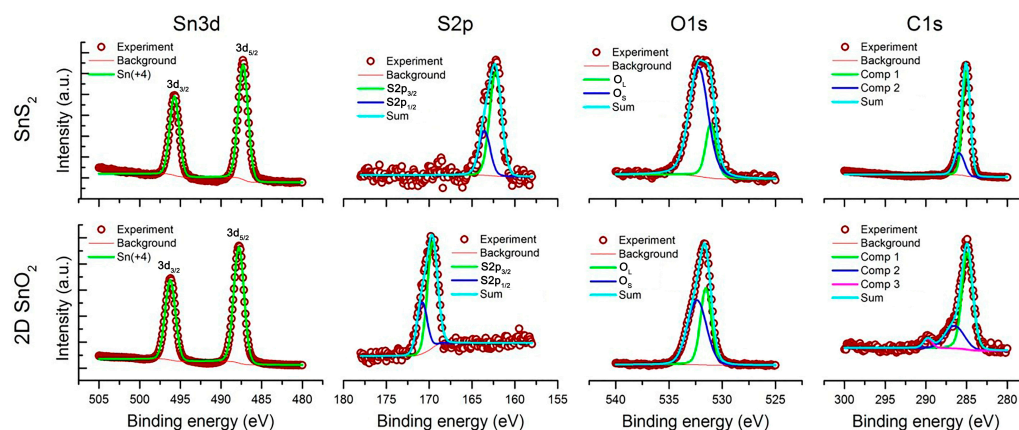


Figure 6. Raman spectra of SnS₂ (a) and 2D SnO₂ (b) samples.

Table 1. Assignments of IR bands and Raman vibrational modes (cm^{-1}).

Sample	IR Band/Region, cm^{-1}	Assignment	Raman Shift, cm^{-1}	Assignment
SnS ₂	400–800	ν (Sn-S) + ν (Sn-O)	230	E _g
	970, 1130	ν (C-O)	317	A _{1g}
	1372	ν_s (COO ⁻)		
	1462, 2852, 2924	ν (C-H)		
	1534	ν_{as} (COO ⁻)		
	1633	ν (C=O)		
	2955	ν (=C-H)		
2D SnO ₂	400–800	ν (Sn-O)	110.5	B _{1g}
	970, 1048, 1122	ν (SO ₄ ²⁻)	270	IR E _u
	1255	δ (CH ₂)	513.5	E _g
	1400	ν_s (COO ⁻)	564.8	surface mode
	1626	δ (H ₂ O) + ν (C=O)	627	A _{1g}
	1728	ν (C=O)	851.7	B _{2g}
	2850–3700	“free” OH groups	997.5	ν (C-C)
			1282.6	δ (CH ₂)
			1609.6	ν (C=O)
			1727.7	ν (C=C)

XP-spectra SnS₂ and 2D SnO₂ are shown in Figure 7. In both cases, tin is present in the oxidation state +4. The positions of the S2p lines correspond to the sulfide anion (162.3 eV, 163.5 eV) in the case of SnS₂, and the sulfate anion (169.6 eV, 170.8 eV) in the case of 2D SnO₂. The ratio of the integral intensities of the sulfur and tin signals is [S]/[Sn] = 0.24 and 0.04 for SnS₂ and 2D SnO₂, respectively. This indicates that in 2D SnO₂, sulfates are surface residues. The O1s spectra contain two components corresponding to oxygen of the oxide (O_L, 530.7–531.2 eV) and oxygen from the surface oxygen-containing species (O_S, 532.0–532.4 eV). The ratio of the integral intensities of oxygen and tin signals [O]/[Sn] = 0.37 and 0.24 for SnS₂ and 2D SnO₂, respectively. Such a large amount of oxygen from oxygen-containing particles on the SnS₂ surface is due to the presence of an organic stabilizer, oleic acid. The C1s spectrum is also complex, and contains two or three components corresponding to the presence of C-C bonds (C1, 284.8–285.0 eV), C-OH and C-O-C bonds (C2, 285.9–286.5 eV) and carboxyl groups COO⁻ (C3, 289.1–289.8 eV). The C3 component appears only in the 2D SnO₂ spectrum. The ratio of the carbon and tin signal-intensities is [C]/[Sn] = 2.22 and 0.04 for SnS₂ and 2D SnO₂, respectively. The main part of the carbon on the surface of the SnS₂ is obviously represented by a long-chain hydrocarbon radical of oleic acid.

**Figure 7.** XP-spectra of SnS₂ and 2D SnO₂.

The FTIR spectra shown in Figure 8 are consistent with the results of the Raman spectroscopy and XPS. The assignment of absorption bands is presented in Table 1 [45].

There are many hydrocarbon fragments and carboxylic groups which may be attributed to oleic acid ligands covering the SnS₂ surface. On the surface of the 2D SnO₂, only residues of the organic-stabilizer oxidation products and sulfate anions were found.

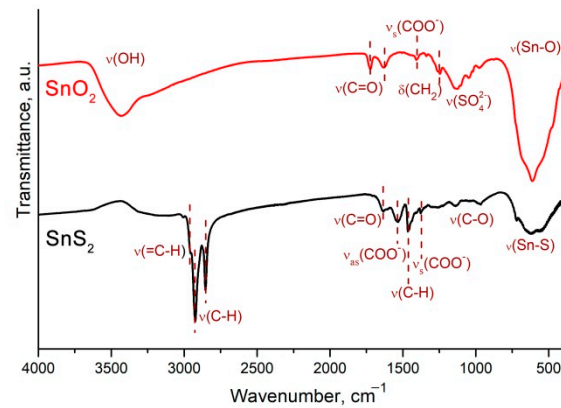
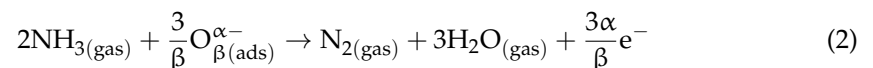
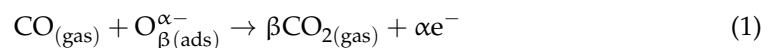


Figure 8. FTIR spectra of SnS₂ and 2D SnO₂ samples.

3.2. Gas Sensor Properties

To evaluate the sensor properties of the 2D SnO₂ model, reducing gases CO (which does not have specific acid-base properties) and NH₃ (which exhibits basic properties) were selected. The measurements were carried out when detecting 20 ppm CO and 20 ppm NH₃ in dry (RH₂₅ = 0%) and humid (RH₂₅ = 30%) air. Examples of changes in the resistance of the 2D SnO₂ when detecting 20 ppm CO and 20 ppm NH₃ in dry air (RH₂₅ = 0%) are shown in Figure 9. The sensor's resistance decreases in the presence of reducing, due to their oxidation by oxygen chemisorbed on the SnO₂ surface:



where CO_(gas), NH_{3(gas)} are CO and NH₃ molecules in the gas phase, O_{β(ads)}^{α-} is the chemisorbed oxygen species (α = 1 and 2 for once- and twice-charged particles, respectively; β = 1 and 2 for atomic and molecular forms, respectively), e⁻ is an electron injected into the conduction band, and CO_{2(gas)}, N_{2(gas)}, H_{2O(gas)} are products of CO and NH₃ oxidation desorbed into the gas phase.

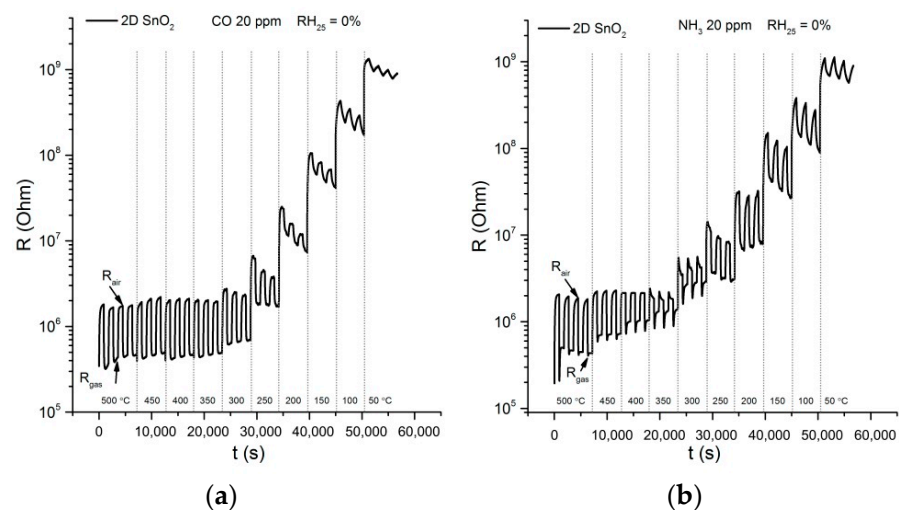


Figure 9. Temperature dependencies of the dynamic-sensor response of 2D SnO₂ when detecting 20 ppm CO (a) and 20 ppm NH₃ (b) in dry air (RH₂₅ = 0%).

In the temperature range 350–500 °C, the independence of the 2D SnO₂ resistance in air on the measurement temperature is observed. Such an unusual type of temperature dependence of the semiconductor resistance may be due to the small thickness of the sensitive layer formed from the sol during the oxidation of the SnS₂ nanosheets. Therefore, the surface of all 2D SnO₂ particles is accessible for oxygen chemisorption, which occurs with electron localization. As a result, the 2D SnO₂ particles with a thickness of several nanometers turn out to be completely depleted of electrons. This corresponds to the situation of the “flat zones”, with the same concentration of electrons in the bulk and near the surface of the crystallite [46], in which the barriers at the grain boundaries that determine the value of the conductivity activation-energy are small. With a decrease in the operating temperature, the thickness of the depleted layer near the 2D SnO₂ surface decreases. This leads to a difference in the electron concentration in the bulk and near the crystallite surface, which leads to the formation of significant surface barriers and a transition to the activation character of conductivity.

At temperatures below 200 °C, baseline drift (the change in resistance in air at the same operating temperature) is observed. This effect may be due to incomplete desorption and accumulation of the products of CO and NH₃ oxidation on the surface of sensitive material.

The temperature dependencies of the sensor’s response are shown in Figure 10. When detecting CO (Figure 10a), there is a significant decrease in the response value. Such a change in signal is apparently because of a decrease in the number of oxidative active-centers on the SnO₂ surface, namely, chemisorbed oxygen anions, which are responsible for the formation of a sensor response when detecting CO [47]. In humid air, dissociative adsorption of water vapor leads to the substitution of both lattice and chemisorbed oxygen by hydroxyl groups [48]. It can be expected that for thin 2D SnO₂ sensitive layers formed from the sol during the oxidation of the SnS₂ nanosheets, the process of surface hydroxylation in humid air occurs to a high extent.

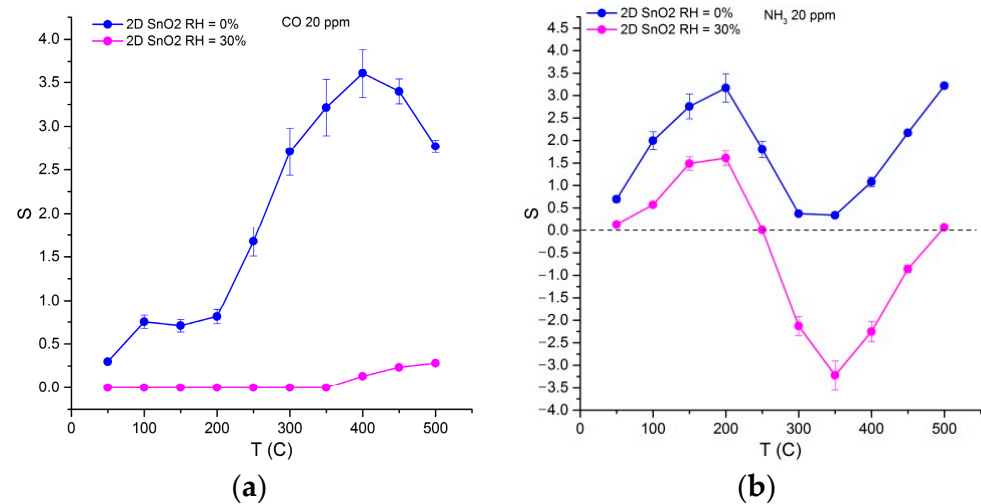


Figure 10. Temperature dependencies of 2D SnO₂ sensor response when detecting 20 ppm CO (a) and 20 ppm NH₃ (b) in dry (RH₂₅ = 0%) and humid (RH₂₅ = 30%) air.

The temperature dependencies of the sensor’s response towards NH₃ have a more complex form (Figure 10b). In dry air, a maximum sensor signal is observed at T = 200 °C. The surface sulfate anions act as additional acid centers, favored for NH₃ adsorption [49]. The temperature range of 250–350 °C corresponds to the minimum sensor response, and a further temperature increase leads to an increase in the sensor signal. When NH₃ is detected in moist air, the sensor response of 2D SnO₂ acquires “negative” values in this temperature range, due to the fact that the resistance of this material in the presence of ammonia becomes greater than in pure air.

Such a change in the response type was reported for various materials: from *n*- to *p*-type for MoO₃ [50], In₂O₃ [51], SnO₂ [52–54], SnO₂(Fe) [55], SnO₂(Pd,Pt) [56], ZnO [57], WO₃ [58,59], TiO₂ [60], and from *p*- to *n*-type conductivity for α -Fe₂O₃ [61], Co₃O₄ [62], graphene [63,64], and SnO₂- and WO₃-decorated graphene [65]. The inversion of the sensor response was explained by different reasons: (i) a change in the type of main charge-carriers in the semiconductor oxide, due to either the surface reactions under certain conditions, or because of the effect of impurities; (ii) kinetic reasons related to the adsorption barrier of the detected gas; (iii) the formation of new donor or acceptor species, which contributes to the change in the sensor conductivity.

The results obtained in this work and in our previous article [54] allow us to conclude that when detecting ammonia, the most likely cause of signal inversion is precisely the appearance of new acceptor species. The reason for the decrease in the SnO₂ response in the temperature range of 250–350 °C is the possible NH₃ to NO oxidation by chemisorbed oxygen. Further interaction of NO molecules with ambient oxygen molecules leads to the formation of surface-bound nitrite and nitrate groups [66]. This process occurs with the localization of charge carriers from the conduction band of the semiconductor, which leads to a decrease in the electrical conductivity of the *n*-type semiconductor material and a formal decrease in the sensor response. The adsorption of water vapor on the SnO₂ surface occurs with an increase in the electron concentration in the conduction band of the semiconductor [48]. This should stimulate the formation of surface nitrite and nitrate groups which occurs with the localization of electrons, and cause a greater increase in the resistance of the sensitive layer.

3.3. In Situ DRIFTS Analysis of 2D SnO₂ Interaction with NH₃

To confirm the above reasoning, the interaction of the 2D SnO₂ with ammonia was investigated using DRIFTS in dry (RH₂₅ = 0%) and humid (RH₂₅ = 30%) air at temperatures of 200 °C and 350 °C, corresponding to the maximum "positive" and maximum "negative" sensor response, respectively. The DRIFT spectra recorded after 100 min exposure in dry or humid air containing 100 ppm NH₃ are shown in Figure 11. Spectra in dry and humid air at 200 °C and 350 °C were used as the baselines.

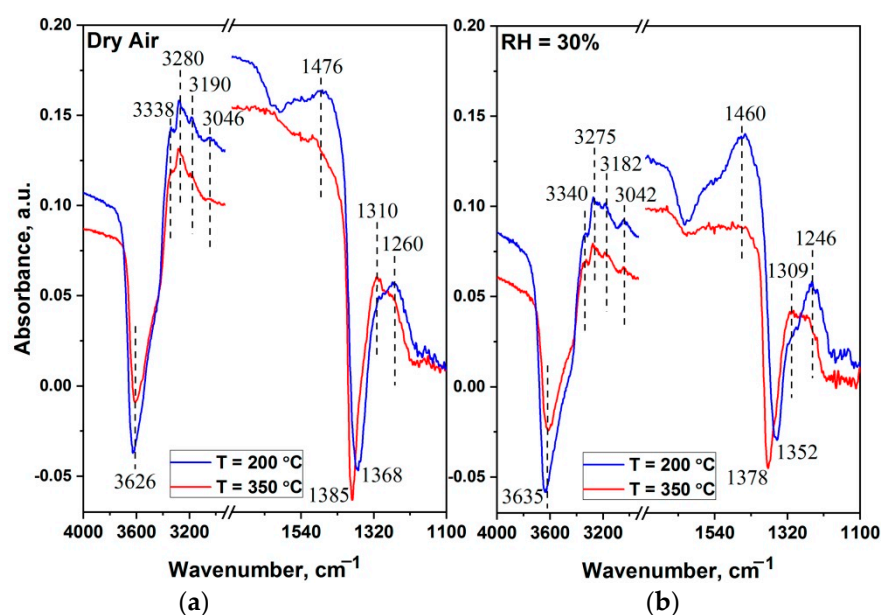


Figure 11. In situ DRIFT spectra of 2D SnO₂ (a) in dry (RH₂₅ = 0%) and (b) in humid (RH₂₅ = 30%) air containing 100 ppm NH₃ at temperatures of 200 °C (blue line) and 350 °C (red line).

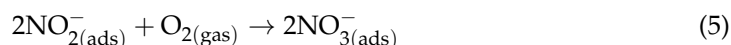
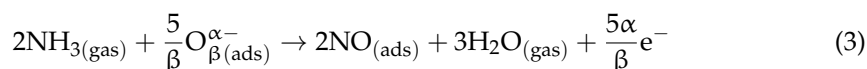
In general, the spectra obtained at 200 °C and 350 °C in dry and humid air are similar (Table 2), but there are also differences corresponding to the type of change in conductivity.

It can be assumed that the adsorption of ammonia molecules proceeds to a greater extent on the Brønsted acid active-sites, which results in a decrease in the intensity of the $\nu(\text{OH})$ and $\delta(\text{H}_2\text{O})$ groups, the protonation of NH_3 and the appearance of bands corresponding to the bending vibrations of NH_4^+ at 1460 and 1476 cm^{-1} . The bands in the range of 1246–1260 cm^{-1} are associated with vibrations of the NH_3^+ coordinated at the Lewis acid sites (tin ions), while the N-H stretching-vibration region of coordinated NH_3 is revealed in the form of many narrow peaks in the range of 3042–3340 cm^{-1} [67,68].

Table 2. Assignments of IR absorption bands (cm^{-1}) appeared in DRFIT spectra on the surface of 2D SnO_2 in dry ($\text{RH}_{25} = 0\%$) and in humid ($\text{RH}_{25} = 30\%$) air containing 100 ppm NH_3 at 200 °C and 350 °C.

Functional Groups	200 °C		350 °C	
	$\text{RH}_{25} = 0\%$	$\text{RH}_{25} = 30\%$	$\text{RH}_{25} = 0\%$	$\text{RH}_{25} = 30\%$
NH_3^+ on Lewis acid site	1258	1246	1268	1260
chelating bidentate nitrate (NO_3^-) or nitrite (NO_2^-)	-	-	1310	1309
SO_2 in ($-\text{SO}_2\cdot\text{NH}-$) or SO_4^{2-}	1368	1352	1385	1378
NH_4^+ on Brønsted acid site	1476	1460	-	-
$\delta(\text{H}_2\text{O})$	1620	1625	-	1625
$\nu(\text{N-H})$ in NH_4^+	3046	3042	3046	3042
$\nu(\text{N-H})$ in NH_3	3185, 3280	3184, 3270	3190, 3280	3189, 3278
$\nu(\text{OH})$	3330–3770	3330–3780	3330–3730	3330–3780

At 200 °C, the presence of intense peaks related to NH_3^+ and NH_4^+ assumes that ammonia is the main reagent interacting with the surface of the sensitive layer of the sensor. Comparing the intensities of these peaks, one can see that a humid atmosphere is a more favorable condition for the adsorption of NH_3 species, at both the Brønsted and Lewis acid sites. At the same time, at 350 °C, a decrease in the intensity of peaks related to the NH_3 species and the appearance of an additional peak at 1310 cm^{-1} can be noticed. The latter corresponds either to chelating bidentate nitrate or chelating bidentate nitrite groups [43,44,69]. The presence of nitrate groups on the surface at high temperature conditions may indicate the oxidation of ammonia molecules to NO (process (3)), and then, with the participation of ambient oxygen, further conversion to NO_2 (processes (4) and (5)). As was shown earlier by Wang et al. [70], the maximum conversion of NO to NO_2 in NH_3 -pre-adsorbed samples is achieved in the temperature range of 350–400 °C.



Processes (4) and (5) can lead to a decrease in the conductivity of the sample, and might be the main reason for the reversing of the sensor signal (Figure 10b). Our results are in agreement with the observations of Zhou et al. [68] and Ramis et al. [71], who observed NH_3 over-oxidation to NO or N_2 at high temperatures above 300 °C.

The appearance of negative IR-adsorption-bands after NH_3 adsorption at the range of 1352–1385 cm^{-1} , depending on the sample, is directly related to the presence of sulfate groups on the surface [43,44]. Hadjiivanov et al. have reported the formation of a negative band in this region, and explained it by the adsorption of species in the immediate vicinity of sulfate anions [72]. Ramis et al. have attributed the negative band at 1362 cm^{-1} to the perturbation of the S=O band of traces of sulphate impurities in $\gamma\text{-Fe}_2\text{O}_3$ [71].

However, it should be noted that this negative absorption-peak also appears during the interaction of ammonia with the sample with pre-adsorbed SO_2 . Thus, according to Zhang et al., the formation of the negative band at 1368 cm^{-1} is associated with the

replacement of the sulfate species by the ammonia ones, while the interaction of SO₂ with the NH₃ pre-treated sample leads to the production of (NH₄)₂SO₄ or NH₄HSO₄ [67].

4. Conclusions

In summary, we have developed a new route to obtain two-dimensional SnO₂ for sensor applications. The 2D SnO₂ nanosheets were successfully synthesized via the oxidation (at 500 °C) of SnS₂ nanosheets obtained in solution during the simple chemical reaction. TEM and SEM data confirmed that the as-grown SnS₂ nanosheets and oxidized SnO₂ nanosheets have 2D morphology. The 2D SnO₂ is characterized by a high specific-surface area and increased surface-acidity, caused by the presence of residual sulfate anions. The combination of these characteristics provides a high 2D SnO₂ sensor signal towards NH₃ at a low temperature of 200 °C in dry air, but at the same time causes an inversion of the sensor response when detecting NH₃ in a humid atmosphere. We have to conclude that SnS₂ nanosheets are a good template for synthesizing 2D SnO₂. Moreover, the features of the active surface-centers formed may be useful when creating sensors for a particular gas with pronounced basic properties. We believe that synthesized 2D SnO₂ will be interesting for the design of new sensitive materials with high sensor performances.

Author Contributions: Conceptualization, R.V., X.L. and M.R.; methodology, R.V., X.L. and M.R.; formal analysis, D.K., V.P. and A.N.; investigation, D.K., N.U., V.P., A.N., T.S. and R.N.; data curation, V.P., A.N. and T.S.; writing—original draft preparation, R.V., D.K., A.N. and M.R.; writing—review and editing, R.V., X.L. and M.R. All authors have read and agreed to the published version of the manuscript.

Funding: This research was funded by the Russian Foundation for Basic Research, grant number 21-53-53018, and the National Natural Science Foundation of China, grant number 62111530055.

Institutional Review Board Statement: Not applicable.

Informed Consent Statement: Not applicable.

Data Availability Statement: The data that support the findings of this study are available from the corresponding author upon reasonable request.

Acknowledgments: TG-MS: FTIR and DRIFTS experiments were carried out using the equipment purchased by funds from the Lomonosov Moscow State University Program of the Development. SEM experiments were carried out using research infrastructure of the “Educational and Methodical Center of Lithography and Microscopy” of Lomonosov Moscow State University, supported by the Interdisciplinary Scientific and Educational School of Moscow State University, “Photonic and Quantum Technologies. Digital Medicine”. TEM experiments were carried out using equipment of the “Nanochemistry and Nanomaterials” center, supported by the Program of Development of Lomonosov Moscow State University. Authors are grateful to Anastasiya Alekseeva (Chemistry Department, Moscow State University) for the XRD investigations.

Conflicts of Interest: The authors declare no conflict of interest.

References

1. Novoselov, K.S.; Geim, A.K.; Morozov, S.V.; Jiang, D.; Zhang, Y.; Dubonos, S.V.; Grigorieva, I.V.; Firsov, A.A. Electric field effect in atomically thin carbon films. *Science* **2004**, *306*, 666–669. [[CrossRef](#)] [[PubMed](#)]
2. Konstantatos, G.; Badioli, M.; Gaudreau, L.; Osmond, J.; Bernechea, M.; Garcia de Arquer, F.P.; Gatti, F.; Koppens, F.H.L. Hybrid graphene–quantum dot phototransistors with ultrahigh gain. *Nat. Nanotech.* **2012**, *7*, 363–368. [[CrossRef](#)] [[PubMed](#)]
3. Liu, X.; Ma, T.; Pinna, N.; Zhang, J. Two-Dimensional Nanostructured Materials for Gas Sensing. *Adv. Funct. Mater.* **2017**, *27*, 1702168. [[CrossRef](#)]
4. Choi, S.-J.; Kim, I.-D. Recent Developments in 2D Nanomaterials for Chemiresistive-Type Gas Sensors. *Electron. Mater. Lett.* **2018**, *14*, 221–260. [[CrossRef](#)]
5. Korotcenkov, G. Black phosphorus—New nanostructured material for humidity sensors: Achievements and limitations. *Sensors* **2019**, *19*, 1010. [[CrossRef](#)]
6. Reich, E.S. Phosphorene Excites Materials Scientists. *Nature* **2014**, *506*, 19. [[CrossRef](#)]
7. Anasori, B.; Lukatskaya, M.R.; Gogotsi, Y. 2D metal carbides and nitrides (MXenes) for energy storage. *Nat. Rev. Mater.* **2017**, *2*, 16098. [[CrossRef](#)]

8. Lee, E.; Kim, D.-J. Recent Exploration of Two-Dimensional MXenes for Gas Sensing: From a Theoretical to an Experimental View. *J. Electrochem. Soc.* **2020**, *167*, 037515. [[CrossRef](#)]
9. Pakdel, A.; Zhi, C.; Bando, Y.; Golberg, D. Low-dimensional boron nitride nanomaterials. *Mater. Today* **2012**, *15*, 256–265. [[CrossRef](#)]
10. Wu, W.; Wang, L.; Li, Y.; Zhang, F.; Lin, L.; Niu, S.; Chenet, D.; Zhang, X.; Hao, Y.; Heinz, T.F.; et al. Piezoelectricity of single-atomic-layer MoS₂ for energy conversion and piezotronics. *Nature* **2014**, *514*, 470–474. [[CrossRef](#)]
11. Andoshe, D.M.; Jeon, J.M.; Kim, S.Y.; Jang, H.W. Two-dimensional transition metal dichalcogenides nanomaterials for solar water splitting. *Electron. Mater. Lett.* **2015**, *11*, 323–335. [[CrossRef](#)]
12. Ou, J.Z.; Ge, W.; Carey, B.; Daeneke, T.; Rotbart, A.; Shan, W.; Wang, Y.; Fu, Z.; Chrimes, A.F.; Wlodarski, W.; et al. Physisorption-Based Charge Transfer in Two-Dimensional SnS₂ for Selective and Reversible NO₂ Gas Sensing. *ACS Nano* **2015**, *9*, 10313–10323. [[CrossRef](#)]
13. Gu, D.; Liu, W.; Wang, J.; Yu, J.; Zhang, J.; Huang, B.; Romyantseva, M.N.; Li, X. Au functionalized SnS₂ nanosheets based chemiresistive NO₂ sensors. *Chemosensors* **2022**, *10*, 165. [[CrossRef](#)]
14. Gu, D.; Wang, X.; Liu, W.; Li, X.; Lin, S.; Wang, J.; Romyantseva, M.N.; Gaskov, A.M.; Akbar, S.A. Visible-light activated room temperature NO₂ sensing of SnS₂ nanosheets based chemiresistive sensors. *Sens. Actuators B Chem.* **2020**, *305*, 127455. [[CrossRef](#)]
15. Alsaif, A.; Field, M.R.; Murdoch, B.J.; Daeneke, T.; Latham, K.; Chrimes, A.F.; Zoolfakar, A.S.; Russo, S.P.; Ou, J.Z.; Kalantarzadeh, K. Substoichiometric two-dimensional molybdenum oxide flakes: A plasmonic gas sensing platform. *Nanoscale* **2014**, *6*, 12780–12791. [[CrossRef](#)] [[PubMed](#)]
16. Bannov, A.; Prasek, J.; Zajickova, L. Investigation of pristine graphite oxide as room-temperature chemiresistive ammonia gas sensing material. *Sensors* **2017**, *17*, 320. [[CrossRef](#)]
17. Kim, T.H.; Kim, Y.H.; Park, S.Y.; Kim, S.Y.; Jang, H.W. Two-dimensional transition metal disulfides for chemoresistive gas sensing: Perspective and challenges. *Chemosensors* **2017**, *5*, 15. [[CrossRef](#)]
18. Neri, G. Thin 2D: The new dimensionality in gas sensing. *Chemosensors* **2017**, *5*, 21. [[CrossRef](#)]
19. Sun, P.; Zhao, W.; Cao, Y.; Guan, Y.; Sun, Y.F.; Lu, G.Y. Porous SnO₂ hierarchical nanosheets: Hydrothermal preparation, growth mechanism, and gas sensing properties. *CrystEngComm* **2011**, *13*, 3718–3724. [[CrossRef](#)]
20. Zhou, Q.; Chen, W.G.; Li, J.; Tang, C.D.; Zhang, H. Nanosheet-assembled flower-like SnO₂ hierarchical structures with enhanced gas-sensing performance. *Mater. Lett.* **2015**, *161*, 499–502. [[CrossRef](#)]
21. Li, T.M.; Zeng, W.; Long, H.W.; Wang, Z.C. Nanosheet-assembled hierarchical SnO₂ nanostructures for efficient gas-sensing applications. *Sens. Actuators B Chem.* **2016**, *231*, 120–128. [[CrossRef](#)]
22. Guo, J.; Zhang, J.; Ju, D.X.; Xu, H.Y.; Cao, B.Q. Three-dimensional SnO₂ microstructures assembled by porous nanosheets and their superior performance for gas sensing. *Powder Technol.* **2013**, *250*, 40–45. [[CrossRef](#)]
23. Zhang, L.X.; Yin, Y.Y. Hierarchically mesoporous SnO₂ nanosheets: Hydrothermal synthesis and highly ethanol-sensitive properties operated at low temperature. *Sens. Actuators B* **2013**, *185*, 594–601. [[CrossRef](#)]
24. Chen, H.; Wang, Q.W.; Kou, C.L.; Sui, Y.M.; Zeng, Y.; Du, F. One-pot synthesis and improved sensing properties of hierarchical flowerlike SnO₂ assembled from sheet and ultra-thin rod subunits. *Sens. Actuators B Chem.* **2014**, *194*, 447–453. [[CrossRef](#)]
25. Lou, Z.; Wang, L.L.; Wang, R.; Fei, T.; Zhang, T. Synthesis and ethanol sensing properties of SnO₂ nanosheets via a simple hydrothermal route. *Solid-State Electron.* **2012**, *76*, 91. [[CrossRef](#)]
26. Zeng, W.; Wu, M.; Li, Y.; Wu, S. Hydrothermal synthesis of different SnO₂ nanosheets with CO gas sensing properties. *J. Mater. Sci. Mater. Electron.* **2013**, *24*, 3701–3706. [[CrossRef](#)]
27. Kakanakova-Georgieva, A.; Giannazzo, F.; Nicotra, G.; Cora, I.; Gueorguiev, G.K.; Persson, P.O.Å.; Pécz, B. Material proposal for 2D indium oxide. *Appl. Surf. Sci.* **2021**, *548*, 149275. [[CrossRef](#)]
28. Dos Santos, R.B.; Rivelino, R.; Gueorguiev, G.K.; Kakanakova-Georgieva, A. Exploring 2D structures of indium oxide of different stoichiometry. *CrystEngComm* **2021**, *23*, 6661–6667. [[CrossRef](#)]
29. Paolucci, V.; De Santis, J.; Lozzi, L.; Giorgi, G.; Cantalini, C. Layered amorphous a-SnO₂ gas sensors by controlled oxidation of 2D-SnSe₂. *Sens. Actuators B Chem.* **2022**, *350*, 130890. [[CrossRef](#)]
30. Paolucci, V.; De-Santis, J.; Ricci, V.; Lozzi, L.; Giorgi, G.; Cantalini, C. Bidimensional Engineered Amorphous a-SnO₂ Interfaces: Synthesis and Gas Sensing Response to H₂S and Humidity. *ACS Sens.* **2022**, *7*, 2058–2068. [[CrossRef](#)]
31. Domingo, G.; Itoga, K.S.; Kannewurf, C.K. Fundamental Optical Absorption in SnS₂ and SnSe₂. *Phys. Rev.* **1966**, *143*, 536–541. [[CrossRef](#)]
32. Takeda, N.; Parkinson, B.A. Adsorption Morphology, Light Absorption, and Sensitization Yields for Squaraine Dyes on SnS₂ Surfaces. *J. Am. Chem. Soc.* **2003**, *125*, 5559–5571. [[CrossRef](#)] [[PubMed](#)]
33. Du, W.M.; Deng, D.H.; Han, Z.T.; Xiao, V.; Bian, V.; Qian, X.F. Hexagonal tin disulfide nanoplatelets: A new photocatalyst driven by solar light. *CrystEngComm* **2011**, *13*, 2071–2076. [[CrossRef](#)]
34. Lei, Y.Q.; Song, S.Y.; Fan, W.Q.; Xing, Y.; Zhang, H.J. Facile Synthesis and Assemblies of Flowerlike SnS₂ and In³⁺-Doped SnS₂: Hierarchical Structures and Their Enhanced Photocatalytic Property. *J. Phys. Chem. C* **2009**, *113*, 1280–1285. [[CrossRef](#)]
35. Shi, W.D.; Huo, L.H.; Wang, H.S.; Zhang, H.J.; Yang, J.H.; Wei, P.H. Hydrothermal growth and gas sensing property of flower-shaped SnS₂ nanostructures. *Nanotechnology* **2006**, *17*, 2918–2924. [[CrossRef](#)]
36. Zhai, C.X.; Du, N.; Zhang, H.; Yang, D.R. Large-scale synthesis of ultrathin hexagonal tin disulfide nanosheets with highly reversible lithium storage. *Chem. Commun.* **2011**, *47*, 1270–1272. [[CrossRef](#)]

37. Kim, T.J.; Kim, C.; Son, D.; Choi, M.; Park, B. Novel SnS₂-nanosheet anodes for lithium-ion batteries. *J. Power Sources* **2007**, *167*, 529–535. [[CrossRef](#)]
38. Seo, J.W.; Jang, J.T.; Park, S.W.; Kim, C.J.; Park, B.W.; Cheon, J.W. Two-Dimensional SnS₂ Nanoplates with Extraordinary High Discharge Capacity for Lithium Ion Batteries. *Adv. Mater.* **2008**, *20*, 4269–4273. [[CrossRef](#)]
39. Mead, D.G.; Irwin, J.C. Raman spectra of SnS₂ and SnSe₂. *Solid State Commun.* **1976**, *20*, 885–887. [[CrossRef](#)]
40. Smith, A.J.; Meek, P.E.; Liang, W.Y. Raman scattering studies of SnS₂ and SnSe₂. *J. Phys. C Solid State Phys.* **1977**, *10*, 1321–1333. [[CrossRef](#)]
41. Gonzales, J.M.; Oleynik, I.I. Layer-dependent properties of SnS₂ and SnSe₂ two-dimensional materials. *Phys. Rev. B* **2016**, *94*, 125443. [[CrossRef](#)]
42. Abello, L.; Bochu, B.; Gaskov, A.; Koudryavtseva, S.; Lucazeau, G.; Rumyantseva, M. Structural characterization of nanocrystalline SnO₂ by X-Ray and Raman Spectroscopy. *J. Solid State Chem.* **1988**, *135*, 78–85. [[CrossRef](#)]
43. Socrates, G. *Infrared and Raman Characteristic Group Frequencies: Tables and Charts*, 3rd ed.; John Wiley & Sons Ltd.: West Sussex, UK, 2001.
44. Diéguez, A.; Romano-Rodriguez, A.; Vilà, A.; Morante, J.R. The complete Raman spectrum of nanometric SnO₂ particles. *J. Appl. Phys.* **2001**, *90*, 1550–1557. [[CrossRef](#)]
45. Nakamoto, K. *Infrared and Raman Spectra of Inorganic and Coordination Compounds. Part A: Theory and Applications in Inorganic Chemistry*, 6th ed.; John Wiley & Sons, Inc.: Hoboken, NJ, USA, 2009.
46. Barsan, N.; Weimar, U. Conduction Model of Metal Oxide Gas Sensors. *J. Electroceramics* **2001**, *7*, 143–167. [[CrossRef](#)]
47. Marikutsa, A.; Rumyantseva, M.; Konstantinova, E.; Gaskov, A. The key role of active sites in the development of selective metal oxide sensor materials. *Sensors* **2021**, *21*, 2554. [[CrossRef](#)]
48. Henrich, V.E.; Cox, P.A. *The Surface Science of Metal Oxides*; Cambridge University Press: Cambridge, UK, 1994.
49. Marikutsa, A.; Sukhanova, A.; Rumyantseva, M.; Gaskov, A. Acidic and catalytic co-functionalization for tuning the sensitivity of sulfated tin oxide modified by ruthenium oxide to ammonia gas. *Sens. Actuators B Chem.* **2018**, *255*, 3523–3532. [[CrossRef](#)]
50. Prasad, A.K.; Kubinski, D.J.; Gouma, P.I. Comparison of sol-gel and ion beam deposited MoO₃ thin film gas sensors for selective ammonia detection. *Sens. Actuators B Chem.* **2003**, *93*, 25–30. [[CrossRef](#)]
51. Korotcenkov, G.; Brinzari, V.; Golovanov, V.; Cerneavschi, A.; Matolin, V.; Todd, A. Acceptor-like behavior of reducing gases on the surface of *n*-type In₂O₃. *Appl. Surf. Sci.* **2004**, *227*, 122–131. [[CrossRef](#)]
52. Epifani, M.; Prades, J.D.; Comini, E.; Cirera, A.; Siciliano, P.; Faglia, G.; Morante, J.R. Chemoresistive sensing of light alkanes with SnO₂ nanocrystals: A DFT-based insight. *Phys. Chem. Chem. Phys.* **2009**, *11*, 3634–3639. [[CrossRef](#)]
53. Brunet, E.; Maier, T.; Mutinati, G.C.; Steinhauer, S.; Köck, A.; Gspan, C.; Grogger, W. Comparison of the gas sensing performance of SnO₂ thin film and SnO₂ nanowire sensors. *Sens. Actuators B Chem.* **2012**, *165*, 110–118. [[CrossRef](#)]
54. Garshev, A.; Ivanov, V.; Krotova, A.; Filatova, D.; Konstantinova, E.; Naberezhnyi, D.; Khmelevsky, N.; Marikutsa, A.; Kots, P.; Smirnov, A.; et al. Enhancement of lewis acidity of Cr-doped nanocrystalline SnO₂ and its effect on surface NH₃ oxidation and the sensory detection pattern. *ChemPhysChem* **2019**, *20*, 1985–1996. [[CrossRef](#)] [[PubMed](#)]
55. Galatsis, K.; Cukrov, L.; Wlodarski, W.; McCormick, P.; Kalantar-zadeh, K.; Comini, E.; Sberveglieri, G. *p*- and *n*-type Fe-doped SnO₂ gas sensors fabricated by the mechanochemical processing technique. *Sens. Actuators B Chem.* **2003**, *93*, 562–565. [[CrossRef](#)]
56. Kutukov, P.; Rumyantseva, M.; Krivetskiy, V.; Filatova, D.; Batuk, M.; Hadermann, J.; Khmelevsky, N.; Aksenenko, A.; Gaskov, A. Influence of Mono- and Bimetallic PtO_x, PdO_x, PtPdO_x Clusters on CO Sensing by SnO₂ Based Gas Sensors. *Nanomaterials* **2018**, *8*, 917. [[CrossRef](#)] [[PubMed](#)]
57. Vorobyeva, N.; Rumyantseva, M.; Konstantinova, E.; Grishina, D.; Gaskov, A. Inversion of NH₃ sensor signal and paramagnetic centers of nanocrystalline ZnO(Ga). *Procedia Eng.* **2011**, *25*, 296–299. [[CrossRef](#)]
58. Shekunova, T.O.; Baranchikov, A.E.; Yapryntsev, A.D.; Rudakovskaya, P.G.; Ivanova, O.S.; Karavanova, Y.A.; Kalinina, M.A.; Rumyantseva, M.N.; Dorofeev, S.G.; Ivanov, V.K. Ultrasonic disintegration of tungsten trioxide pseudomorphs after ammonium paratungstate as a route for stable aqueous sols of nanocrystalline WO₃. *J. Mater. Sci.* **2018**, *53*, 1758–1768. [[CrossRef](#)]
59. Wu, Y.-Q.; Hu, M.; Wei, X.-Y. A study of transition from *n*- to *p*-type based on hexagonal WO₃ nanorods sensor. *Chin. Phys. B* **2014**, *23*, 40704. [[CrossRef](#)]
60. Kim, I.-D.; Rothschild, A.; Lee, B.H.; Kim, D.Y.; Jo, S.M.; Tuller, H.L. Ultrasensitive Chemiresistors Based on Electrospun TiO₂ Nanofibers. *Nano Lett.* **2006**, *6*, 2009–2013. [[CrossRef](#)]
61. Gurlo, A.; Sahm, M.; Oprea, A.; Barsan, N.; Weimar, U. A *p*- to *n*-transition on α-Fe₂O₃-based thick film sensors studied by conductance and work function change measurements. *Sens. Actuators B Chem.* **2004**, *102*, 291–298. [[CrossRef](#)]
62. Vladimirova, S.; Krivetskiy, V.; Rumyantseva, M.; Gaskov, A.; Mordvinova, N.; Lebedev, O.; Martyshov, M.; Forsh, P. Co₃O₄ as *p*-type material for CO sensing in humid air. *Sensors* **2017**, *17*, 2216. [[CrossRef](#)]
63. Pearce, R.; Iakimov, T.; Andersson, M.; Hultman, L.; Lloyd Spetz, A.; Yakimova, R. Epitaxially grown graphene based gas sensors for ultra sensitive NO₂ detection. *Sens. Actuators B Chem.* **2011**, *155*, 451–455. [[CrossRef](#)]
64. Jaaniso, R.; Kahro, T.; Kozlova, J.; Aarik, J.; Aarik, L.; Alles, H.; Floren, A.; Gerst, A.; Kasikov, A.; Niilisk, A.; et al. Temperature induced inversion of oxygen response in CVD graphene on SiO₂. *Sens. Actuators B Chem.* **2014**, *190*, 1006–1013. [[CrossRef](#)]
65. Behi, S.; Bohli, N.; Casanova-Cháfer, J.; Llobet, E.; Abdelghani, A. Metal Oxide Nanoparticle-Decorated Few Layer Graphene Nanoflake Chemoresistors for the Detection of Aromatic Volatile Organic Compounds. *Sensors* **2020**, *20*, 3413. [[CrossRef](#)] [[PubMed](#)]

66. Yang, L.; Marikutsa, A.; Romyantseva, M.; Konstantinova, E.; Khmelevsky, N.; Gaskov, A. Quasi similar routes of NO₂ and NO sensing by nanocrystalline WO₃: Evidence by in situ DRIFT spectroscopy. *Sensors* **2019**, *19*, 3405. [[CrossRef](#)] [[PubMed](#)]
67. Zhang, Z.; Chen, L.; Li, Z.; Li, P.; Yuan, F.; Niu, X.; Zhu, Y. Activity and SO₂ resistance of amorphous Ce_aTiO_x catalysts for the selective catalytic reduction of NO with NH₃: In situ DRIFT studies. *Catal. Sci. Technol.* **2016**, *6*, 7151. [[CrossRef](#)]
68. Zhou, G.; Zhong, B.; Wang, W.; Guan, X.; Huang, B.; Ye, D.; Wu, H. In situ DRIFTS study of NO reduction by NH₃ over Fe–Ce–Mn/ZSM-5 catalysts. *Catal. Today* **2011**, *175*, 157–163. [[CrossRef](#)]
69. Hadjiivanov, K.I. Identification of neutral and charged N_xO_y surface species by IR spectroscopy. *Catal. Rev. Sci. Eng.* **2000**, *42*, 71–144. [[CrossRef](#)]
70. Wang, D.; Zhang, L.; Kamasamudram, K.; Epling, W.S. In Situ-DRIFTS Study of Selective Catalytic Reduction of NO_x by NH₃ over Cu-Exchanged SAPO-34. *ACS Catal.* **2013**, *3*, 871–881. [[CrossRef](#)]
71. Ramis, G.; Yi, L.; Busca, G.; Turco, M.; Kotur, E.; Willey, R.J. Adsorption, Activation, and Oxidation of Ammonia over SCR Catalysts. *J. Catal.* **1995**, *157*, 523–535. [[CrossRef](#)]
72. Hadjiivanov, K.; Avreyska, V.; Klissurski, D.; Marinova, T. Surface Species Formed after NO Adsorption and NO + O₂ Coadsorption on ZrO₂ and Sulfated ZrO₂: An FTIR Spectroscopic Study. *Langmuir* **2002**, *18*, 1619–1625. [[CrossRef](#)]